Monthly Notices
of the
ROYAL ASTRONOMICAL SOCIETY

Mon. Not. R. Astron. Soc. **402,** 1126–1140 (2010) doi:10.1111/j.1365-2966.2009.15940.x

High-precision astrometry with MICADO at the European Extremely Large Telescope

S. Trippe,[1⋆] R. Davies,[2] F. Eisenhauer,[2] N. M. Förster Schreiber,[2] T. K. Fritz[2] and R. Genzel[2,3]

[1] *Institut de Radioastronomie Millimétrique, 300 rue de la Piscine, F-38406 Saint Martin d'Hères, France*
[2] *Max-Planck-Institut für extraterrestrische Physik, Giessenbachstrasse 1, D-85748 Garching, Germany*
[3] *Department of Physics, Le Conte Hall, University of California, Berkeley, CA 94720, USA*

Accepted 2009 October 26. Received 2009 October 26; in original form 2009 September 11

ABSTRACT

In this article, we identify and discuss various statistical and systematic effects influencing the astrometric accuracy achievable with Multi-adaptive optics Imaging CAmera for Deep Observations, the near-infrared (NIR) imaging camera proposed for the 42-m European Extremely Large Telescope. These effects are instrumental (e.g. geometric distortion), atmospheric (e.g. chromatic differential refraction) and astronomical (reference source selection). We find that there are several phenomena having impact on $\sim$100 μas scales, meaning they can be substantially larger than the theoretical statistical astrometric accuracy of an optical/NIR 42-m telescope. Depending on type, these effects need to be controlled via dedicated instrumental design properties or via dedicated calibration procedures. We conclude that if this is done properly, astrometric accuracies of 40 μas or better – with 40 μas yr^{-1} in proper motions corresponding to $\approx$20 km s^{-1} at 100 kpc distance – can be achieved in one epoch of actual observations.

Key words: instrumentation: high angular resolution – techniques: high angular resolution – telescopes – astrometry.

1 INTRODUCTION

The future optical/near-infrared (NIR) European Extremely Large Telescope (E-ELT; see e.g. Gilmozzi & Spyromilio 2008), which is designed with a 42-m aperture, will offer a substantial improvement in angular resolution compared to existing facilities. At wavelengths $\lambda = 2\,\mu$m, diffraction-limited resolutions of $\Theta \simeq 10$ mas will be achieved. In terms of angular resolution in the NIR, the E-ELT will outperform existing 8–10-m class telescopes like the Very Large Telescope (VLT) or Keck by factors of $\approx$4–5 and the future James Webb Space Telescope by factors of $\approx$7. This increase in angular resolution should translate into a corresponding improvement in astrometric accuracy.

In order to exploit the E-ELT's resolution, a German–Dutch–Italian–French consortium[1] proposed the Multi-adaptive optics Imaging CAmera for Deep Observations (MICADO) in 2008 February. As the spatial resolution of any ground-based observatory is initially limited by the atmospheric seeing, MICADO will be equipped with a multiconjugate adaptive optics (MCAO) system for achieving the diffraction limit of the 42-m telescope. This system uses three natural and six laser guide stars for correcting the atmospheric turbulence in a wide (>2 arcmin) FOV (Diolaiti et al. 2008). Images will be recorded by an array of 4 × 4 NIR Hawaii-4RG detectors with 4096 × 4096 pixels each, covering a FOV of 53 arcmin. The instrument is sensitive to the wavelength range 0.8–2.5 μm, thus covering the *I, Y, J, H, K* bands. For astrometric experiments, the use of the data analysis software ASTRO-WISE (Valentijn et al. 2007) is foreseen.

In order to achieve its science goals (see Section 2 for details), MICADO needs to reach a stable (time-scales of years) astrometric accuracy of approximately 50 μas. At present 8–10-m class telescopes, accuracies of $\approx$0.5 per cent of a resolution element can be reached regularly (e.g. Fritz et al. 2009). Therefore, from simple scaling of results our goal a priori appears reasonable. However, at levels of the order of 100 μas there are several sources of statistical and systematic errors which need to be taken into account carefully. In this article, we discuss those effects and analyse strategies to bypass them. We conclude that reaching an astrometric accuracy of better than 50 μas is highly challenging in terms of instrument design and data calibration but feasible.

MICADO's astrometric performance should be of the same magnitude as that of the future astrometry space mission *Gaia* (e.g. Jordan 2008). *Gaia* will achieve accuracies better than $\approx$50 μas

⋆E-mail: trippe@iram.fr

[1] The MICADO collaboration includes: MPE Garching, Germany; USM Munich, Germany; MPIA Heidelberg, Germany; NOVA (a collaboration of the universities of Leiden, Groningen and ASTRON Dwingeloo), the Netherlands; OAPD Padova (INAF), Italy; LESIA Paris, France.

only for bright ($V < 15.5$) targets and only at the end of its mission. MICADO is expected to achieve this accuracy for targets with $K_{AB} < 26$. Other space missions like the Space Interferometry Mission (SIM) PLANETQUEST (e.g. Edberg et al. 2007) or JASMINE (e.g. Yano et al. 2007) also aim specifically at bright targets in order to reach accuracies of ≈10 μas (at the best).

For illustration purposes, Fig. 1 shows simulated observations of the nuclear star cluster of the Milky Way using both present day 8–10-m class telescopes and E-ELT/MICADO. Physical parameters of the star cluster (stellar density profile, luminosity function) are taken from Genzel et al. (2003). We discuss technical details of our simulations in Section 4.1. These maps demonstrate the impressive progress to be expected with MICADO.

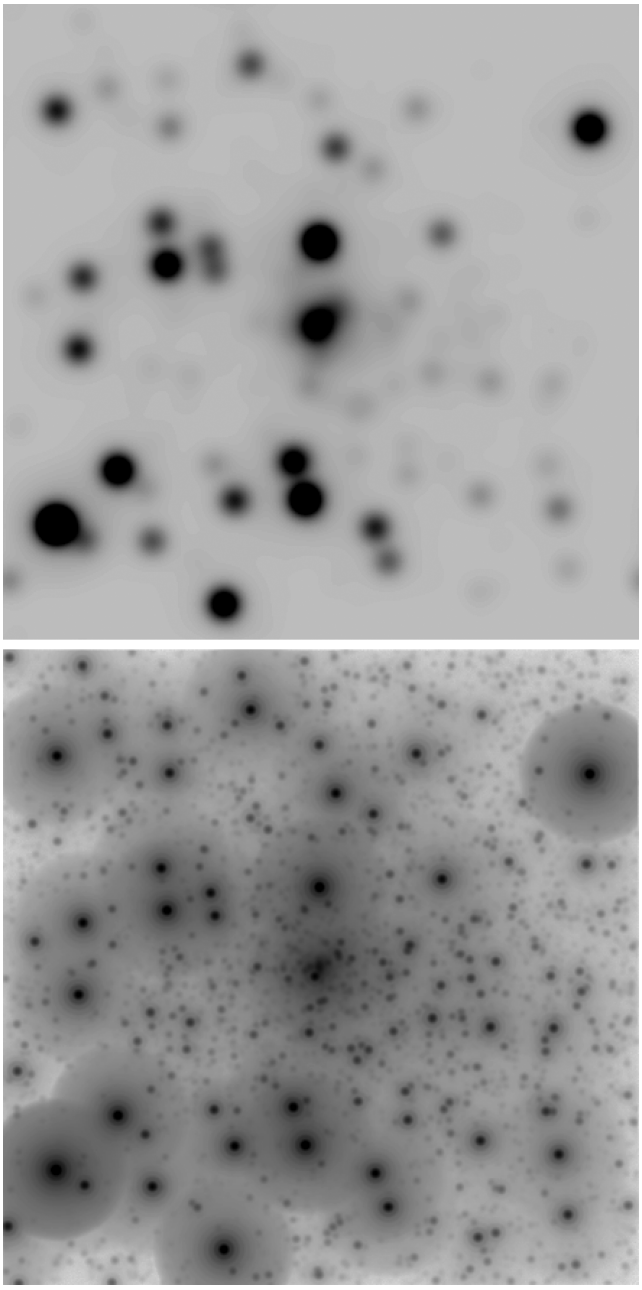

Figure 1. An illustration of the expected performance of the E-ELT/MICADO system. These simulated maps show the central 1×1 arcsec^2 (i.e. 8000×8000 au) of the nuclear star cluster of the Milky Way at 2.2 μm. Top panel: the target region as observed with present day 8–10-m class telescopes. The diffraction-limited resolution is ≈50 mas. For comparison with actual observations, see e.g. Genzel et al. (2003), Ghez et al. (2005). Bottom panel: the same field as seen by MICADO. The angular resolution is ≈10 mas. The improvement in detail and depth is obvious.

Although this study is set up for the specific case of MICADO, most of its results are valid in general and therefore of interest beyond the E-ELT community.

This paper is organised as follows. In Section 2, we discuss the science cases identified for MICADO. In Section 3, we review the concepts and techniques of accurate astrometry. In Section 4, we identify and analyse sources of systematic errors one by one and describe methods for minimizing those errors. We provide a summary of our results and an overall error budget in Section 5 and present our conclusions in Section 6.

2 SCIENCE CASES

As part of the instrument design study, the MICADO collaboration has identified and analysed (Renzini 2008, and references therein) several science cases for which the high astrometric accuracy of E-ELT/MICADO is crucial and promises major discoveries. We discuss them in the following one by one.

2.1 Galactic Centres

Located at a distance of ≈8 kpc, the nuclear region of the Milky Way is the closest galactic nucleus, hosting the supermassive black hole ($M_\bullet \approx 4 \times 10^6\,M_\odot$) Sgr A* (e.g. Gillessen et al. 2009). It is therefore a unique laboratory for exploring the regime of strong gravity, accretion on to black holes, and the co-evolution of dense star clusters and active galactic nuclei.

Present-day NIR instrumentation, e.g. VLT/Nasmyth Adaptive Optics System (NAOS)/Coude Near-Infrared Camera (CONICA) (NACO), provides astrometric accuracies down to ≈0.3 mas and angular resolutions down to ≈50 mas (e.g. Fritz et al. 2009). This allowed to identify several stars on Keplerian orbits around Sgr A* with orbital periods down to ≈15 years and pericentre distances as small as ≈100 au (≈12 mas on sky; e.g. Gillessen et al. 2009). It made possible to study in detail the kinematics and the composition of the nuclear star cluster in the gravitational potential of the central black hole. With E-ELT/MICADO, one can expect to achieve sensitivities that are more than 5-mag fainter than for VLT/NACO. Angular resolutions and astrometric accuracies should also improve by factors of about 5, meaning that proper motions of order 10 μas yr^{-1} (400 m s^{-1}) can be detected within few years of observations. Such instrumental performance is necessary in order to address several new questions (e.g. Gillessen et al. 2009).

(i) Identification of stars on close by Keplerian orbits with periods of few years.

(ii) Measuring the *prograde* relativistic orbit precession and testing other effects of general relativity.

(iii) Probing possible *retrograde* orbit precession due to an extended mass component built from compact stellar remnants.

(iv) Analysing the various separate kinematic structures of the nuclear star cluster, and searching for new ones.

(v) Quantifying the binary star fraction in the nuclear cluster.

With MICADO, this type of analysis can be extended to other nearby galaxies. One obvious example is the core of M31 which hosts a $M_\bullet \approx 1.4 \times 10^8_\odot$ black hole. Similar to the case of the Milky Way, M31's nucleus shows several distinct stellar populations: a triple nucleus and two nested star discs around the central

black hole have been identified (Bender et al. 2005). Although M31 is more distant from earth by a factor of ≈100 compared to the Galactic Centre, the larger mass of its black hole (by a factor of ≈35) causes stellar proper motions of about 6 per cent compared to those in the nuclear cluster of the Milky Way. Therefore, kinematic analyses analogous to the Galactic Centre experiment will require capabilities as predicted for E-ELT/MICADO.

Another example is Centaurus A which hosts a $M_\bullet \approx 5 \times 10^7_\odot$ black hole (Neumayer et al. 2007). Given its distance of ≈5 Mpc, proper motions of ≈10 μas yr^{-1} correspond to ≈200 km s^{-1}. Thus, measuring the motions of stars in the vicinity of the black hole is possible. Other galaxies might be interesting targets as well.

2.2 Intermediate-mass black holes

The expected high astrometric accuracy of MICADO opens a new window in the search for and analysis of intermediate-mass black holes (IMBH), objects with masses of few thousand solar masses. In the last years, the detection of those objects in the Arches cluster (Portegies Zwart et al. 2006), the star association GCIRS13 in the Galactic Centre (e.g. Maillard et al. 2004), ω Cen (Noyola, Gebhard & Bergmann 2008), and other locations has been claimed. Most of these analyses are based on radial velocity dispersion profiles. This introduces systematic ambiguities as anisotropic velocity dispersions can mimic the presence of central point masses; this effect can be seen, for example, in the anisotropy term in the Jeans equation. Therefore, reliable (non-)detections of IMBHs require measurements of stellar proper motions (e.g. Anderson & van der Marel 2009). Typical velocity dispersions σ_* of star clusters are of the order of 10 km s^{-1}. This corresponds to ≈50 μas yr^{-1} at a distance of 40 kpc, meaning that for most of the Galactic star clusters a proper motion analysis is feasible with MICADO only. This allows

(i) constraining black hole masses in Galactic star clusters within few years,
(ii) probing the low-mass end of the $M_\bullet - \sigma_*$ relation and
(iii) testing the dynamical evolution of star clusters.

2.3 Globular clusters

As discussed above, the astrometric accuracy of MICADO should allow measuring stellar proper motions of few km s^{-1} for most Galactic globular clusters. Additionally, direct measurements of cluster parallaxes become possible: for a distance of 40 kpc, the full parallax displacement is 50 μas, corresponding to MICADO's predicted astrometric accuracy. This allows addressing several topics.

(i) The spatial distribution of globular clusters.
(ii) Cluster proper motions and their orbits around the Milky Way (e.g. Bedin et al. 2003, 2006).
(iii) Internal cluster kinematics, including rotation.
(iv) Separating cluster members from field stars, thus making analyses of cluster star populations more reliable (see also Anderson et al. 2006).

2.4 Dark matter in dwarf spheroidal galaxies

Cold dark matter models predict high-mass densities and cuspy density profiles for the central regions of galaxy haloes. In contrast, warm dark matter models predict substantially lower central densities and constant density cores at small radii. The dwarf spheroidal satellite galaxies of the Milky Way provide a unique laboratory to test those models. Their proximity of ≈100 kpc makes it possible to resolve individual stars and analyse their dynamics in the gravitational potentials of their galaxies. Present-day studies are usually based on line-of-sight velocity dispersion profiles. However, there are degeneracies of velocity dispersion anisotropies with mass density profiles. Therefore, any conclusive analysis requires measuring all three components of the velocity vectors of the tracer stars (e.g. Strigari, Bullock & Kaplinghat 2007).

This type of studies requires accurate proper motion measurements with uncertainties of few km s^{-1} or better. MICADO will be able to provide accuracies of ≈5 km s^{-1} within few years of observations for targets about 100 kpc away. This makes MICADO a decisive tool for testing the validity of present-day dark matter models.

3 THE ASTROMETRY PROBLEM

Throughout this paper, we use the term 'astrometry' the following way. We discuss time-resolved *relative* positions, meaning the positions of a science target with respect to a set of reference sources. Science target and reference sources are located in the field of view (FOV) of the camera, i.e. they are recorded simultaneously in the same science image.

Intra-epoch measurements cover timelines that are so short that intrinsic motions of science targets or reference sources cannot be detected. This can be a set of images taken within the same night or a few adjacent nights. Any variations in measured positions are due to measurement errors and can be used to determine the position accuracies. All information obtained from this data set (i.e. images, coordinates, etc.) can be combined, e.g. for improving the signal-to-noise ratio (SNR).

Inter-epoch measurements cover timelines sufficient for detecting source motions. Those data cannot be combined in a straight forward manner. Intrinsic source motions and measurement errors interfere and need to be disentangled, usually meaning that calculating errors requires additional information. Given MICADO's proper motion accuracies of ≈50 μas yr^{-1} or better (depending on the duration of the experiments), corresponding to ≈10 km s^{-1} at 40 kpc distance, intrinsic motion of Galactic stars is detected easily. Therefore, it will be necessary to use extragalactic sources, including high-redshift objects like quasi-stellar objects (QSOs), as references for some science cases.

If a set of science images is at hand, the general analysis recipe is as follows.

Step 1. From each image n, one extracts the detector positions $\{\boldsymbol{X}^n\}$ of all sources of interest (science targets and reference sources). Detector positions need to be measured with high accuracies of the order of few millipixels (mpix). Existing centroiding, source profile fitting, and point spread function (PSF) correlation algorithms provide such accuracies (e.g. Berry & Burnell 2000; Diolaiti et al. 2000; Trippe 2008).

Step 2. For each image n, the detector positions $\{\boldsymbol{X}^n\}$ need to be converted into global astrometric coordinates $\{\boldsymbol{X}^n\}$. The reference frame can be the detector coordinates of a selected zero-point image or any more general astrometric coordinate system. Using the detector positions of the reference sources $\{\boldsymbol{X}^n_{\rm ref}\}$ and their astrometric positions $\{\boldsymbol{X}^n_{\rm ref}\}$, one calculates a transformation

$$\mathsf{T}_n : \left\{\boldsymbol{X}^n_{\rm ref}\right\} \longrightarrow \left\{\boldsymbol{x}^n_{\rm ref}\right\}. \quad (1)$$

Obtaining the positions $\{\boldsymbol{x}^n_{\rm ref}\}$ requires some prior knowledge on the reference sources. One powerful approach is cross-calibration with other data sets, may be from other wavelength regimes. A nice example is given by Reid et al. (2007). They use precise very long baseline interferometry (VLBI) astrometry of SiO maser stars in

order to define an astrometric reference frame in K-band images of the Galactic Centre.

If the reference sources are known to be not moving (e.g. extragalactic objects), one can set $\{\boldsymbol{x}^n_{\rm ref}\} = \{\boldsymbol{X}^0\}$; the index 0 indicates the selected zero-point in time. The same can be done if the reference source ensemble is (or is defined as being) at rest *in average*, i.e. $\langle\{\boldsymbol{x}^0_{\rm ref}\}\rangle = \langle\{\boldsymbol{x}^n_{\rm ref}\}\rangle$ (e.g. a sufficiently large set of stars in a star cluster). In this case, however, one will loose information on a global motion (drift, rotation, contraction, etc.) of the combined system 'science target + reference sources'. In any case, the transformation $\mathbf{T}_n$ is used to compute global astrometric coordinates for the science targets like

$$\{\boldsymbol{X}^n\} \longrightarrow \mathbf{T}_n\,(\{\boldsymbol{X}^n\}) = \{\boldsymbol{x}^n\}. \tag{2}$$

Commonly, low-order (<5) two-dimensional polynomial coordinate transformations

$$x' = a_0 + a_1x + a_2y + a_3x^2 + a_4y^2 + a_5xy + \cdots, \tag{3}$$

$$y' = b_0 + b_1x + b_2y + b_3x^2 + b_4y^2 + b_5xy + \cdots \tag{4}$$

are used. In case prior knowledge on the geometry of the required transformation is available, one can use models with smaller numbers of free parameters (e.g. Montenbruck & Pfleger 1989; Anderson et al. 2006; Trippe et al. 2008).

The number of available reference sources governs the maximum order of coordinate transformations (see step 2). A first-order polynomial transform with six parameters requires three reference sources, i.e. $2 \times 3 = 6$ coordinates. A second-order transform (12 parameters) requires six reference sources, and so on. Throughout this paper, we assume that *any two science images need to be connected via full astrometric transformations*. This means that we regard more simple methods of data combination like stacking, simple-shift-and-add, etc. as non-astrometric and thus not usable for our purpose.

In order to judge the astrometric accuracy achievable with a system like MICADO, one has to distinguish statistical and systematic influences. The *statistical* measurement accuracy is given by

$$\sigma_L = \frac{\lambda}{\pi D}\frac{1}{\rm SNR} = 284\,\mu{\rm as}\left(\frac{\lambda}{2.17\,\mu{\rm m}}\right)\left(\frac{5\,{\rm m}}{D}\right)\left(\frac{100}{\rm SNR}\right). \tag{5}$$

Here, λ is the wavelength, D is the telescope aperture and SNR is the signal-to-noise ratio (Lindegren 1978). To give an example for the case of the E-ELT: with $\lambda = 2.2$ μm (K-band), $D = 42$ m and SNR = 100, one obtains a statistical astrometric accuracy $\sigma_L = 34$ μas. From this, we see that – in principle – astrometric accuracies of ∼10 μas can be obtained with the E-ELT. This means that any source of additional, especially *systematic* error, needs to be compensated down to this level if one actually wants to fully exploit the E-ELT's capabilities.

4 ERROR SOURCES

In total, we have identified 10 effects that might have the potential to reduce the expected astrometric accuracy of MICADO substantially. We will discuss these 'Terrible Ten' in the following sections. The first three phenomena we analyse are instrumental, the next five are atmospheric and the last two are astronomical.

4.1 Sampling and pixel scales

The detector position of a point source can be computed only if the source PSF is sufficiently sampled. If the pixel scale – expressed in angular units per pixel – is too large (undersampling), position information is lost because there is no unique mathematical description for the PSF profile anymore. Especially, a PSF can then be modelled by profiles with different centres of light (i.e. different detector positions). This effect is known as the *pixel phase error*. It can reach magnitudes of several tenths of a pixel, thus providing an important boundary condition for the instrument design. A detailed description of this phenomenon is provided by Anderson & King (2000).

Table 1. Strehl ratio estimates as obtained from preliminary simulations (Liske 2008; Kissler-Patig, private communication). The $\lambda_{\rm centre}$ are the central wavelengths of the filters.

Band	*I*	*J*	*H*	*K*
$\lambda_{\rm centre}$ (μm)	0.900	1.215	1.654	2.179
Strehl ratio (per cent)	2	18	35	53

In order to identify the critical pixel scale of MICADO, we first created artificial PSFs for each of the bands *I, J, H* and *K*. We modelled each PSF $P(\boldsymbol{x})$ as a superposition of a two-dimensional Airy function $A(\boldsymbol{x})$ and a two-dimensional Moffat profile $M(\boldsymbol{x})$ like

$$P(\boldsymbol{x}) = aA(\boldsymbol{x}) + (1-a)M(\boldsymbol{x}). \tag{6}$$

For each PSF, a stochastic optimization routine[2] adjusted the parameter $a \in [0, 1]$ such that the resulting PSF profile showed the proper Strehl ratio. We took Strehl ratio estimates for MICADO from preliminary E-ELT adaptive optics (AO) system simulations (Liske 2008; Kissler-Patig, private communication), the values are shown in Table 1.

For each of the four wavelength bands, we examined pixel scales from 1 to 7 mas pix^{-1} in steps of 0.1 mas pix^{-1}. In each configuration, we placed the PSF at a random detector position and rebinned it to the corresponding pixel scale. After this, we fit the detector position with a two-dimensional Gaussian light distribution. We iterated this procedure 250 times for each configuration. Pixel phase errors were the rms values of the distributions of the differences between true and measured positions.

The results of our analysis are shown in Fig. 2. For clarity, we restrict the diagram to the decisive pixel scale range from 2 to 4 mas pix^{-1}. For all wavelength bands, the errors are smaller than ≈1 μas for pixel scales below 3 mas pix^{-1}. Given that the filter bands span a factor of 2.4 in wavelength and thus in λ/D, it might not be obvious why the critical pixel scales we find are that similar for all bands. This effect is caused by the differences in Strehl ratios: whereas, the diffraction-limited profile width decreases with decreasing wavelength the Strehl ratio decreases too, meaning a stronger atmospheric blur. In our case, the two effects roughly counterbalance each other; we actually find the smallest beam size for the H-band PSF due to its combination of high SNR (≈35 per cent) and small diffraction limit ($\lambda/D \approx 8.1$ mas). This makes it possible to quote a single critical pixel scale for all bands. We therefore conclude that for *isolated* point sources pixel scales up to 3 mas pix^{-1} can be used for MICADO without introducing notable (≈1 μas) pixel phase errors. Therefore, we use this scale as the standard value for the MICADO design.

In case of *crowding*, the astrometric accuracy is additionally limited by source overlap. For this reason, the MICADO design

[2] Implemented in the MPE data processing software DPUSER developed by Thomas Ott; see http://www.mpe.mpg.de/∼ott/dpuser/history.html

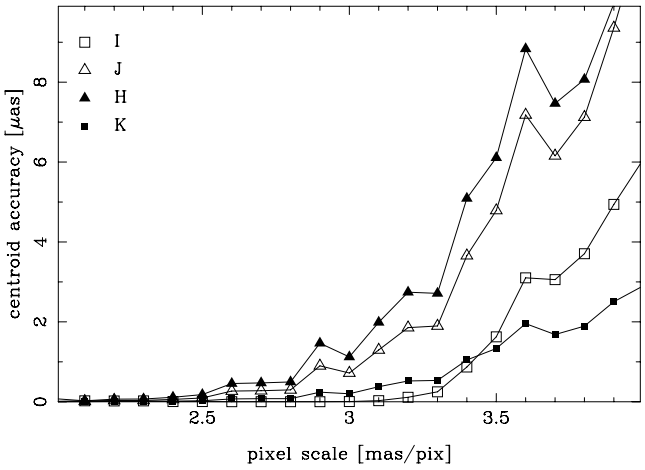

Figure 2. Pixel phase error versus pixel scale for *I, J, H, K* bands for *isolated* sources. Model PSFs are superpositions of Airy and Moffat profiles with Strehl ratios as given in Table 1. For all bands, the errors are below ≈1 μas for pixel scales smaller than 3 mas pix^{-1}.

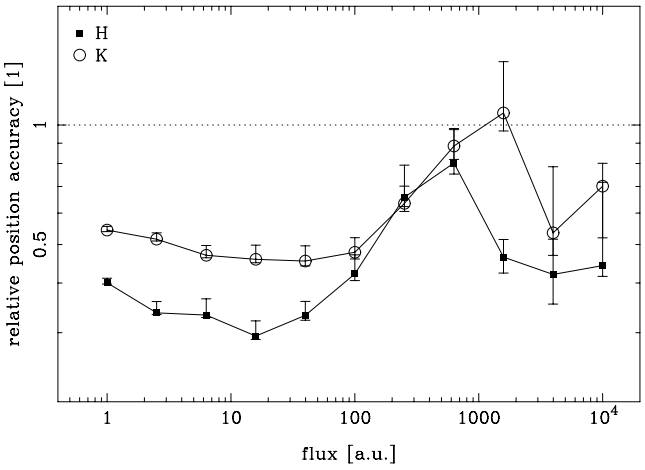

Figure 3. Relative median astrometric error versus source flux for *crowded* sources, separately for *H* and *K* bands. The results for the pixel scales 1.5 mas pix^{-1} are given as fractions of the uncertainties found for 3 mas pix^{-1}. The horizontal dashed line indicates a ratio of 1. Error bars indicate the 68 per cent uncertainty ranges. This analysis shows that reducing the pixel scale improves the typical accuracies by factors of ≈2–3.

foresees a 'small-scale mode'. As the camera design is catoptric and all mirrors are fixed, we use a pick-up arm to image a small (6 arcsec, using one out of the 4 × 4 detectors) FOV with a reduced pixel scale of 1.5 mas pix^{-1}. The reduced scale helps to better separate close by sources and such reduce the misplacements of the source centroids.

In order to quantify this effect, we examined our two pixel scales, 1.5 and 3 mas pix^{-1}, for each of the bands *H* and *K*, meaning four configurations in total. For each configuration, we simulated a crowded star field by placing PSFs at random positions. We used the same model PSFs as for the case of isolated sources. We applied a luminosity profile corresponding to the *K*-band luminosity function of the Galactic bulge which is d log n/d log $S \approx -0.8$ (Zoccali et al. 2003; n is the source number, S is the flux). The dynamic range of the star sample was 10 mag, i.e. a factor of 10 000 in flux. Source densities were ≈3000 stars arcsec^{-2}. We also used these routines (with modified parameters) to create the map shown in Fig. 1.

In each simulated map, we searched for stars and calculated their detector positions using the PSF fitting routine STARFINDER (Diolaiti et al. 2000). We derived median uncertainties versus fluxes from the distributions of the differences between true and measured positions. As the absolute values of these errors are functions of several parameters like fluxes, luminosity profiles and source densities, we converted our results into relative numbers, using the errors obtained for the 3 mas pix^{-1} scales as references.

The outcome of our analysis is presented in Fig. 3. Reducing the pixel scales from 3 to 1.5 mas pix^{-1} improves the typical accuracies by factors of ≈2–3. The effect is stronger in *H* than in *K* band; this indicates that images with smaller beam sizes profit more from a small pixel scale. For the brightest sources (more than ≈500 units), the differences between the pixel scales are (at least in *K* band) not very pronounced any more because (i) the number of very bright sources is small and (ii) they outshine most of their neighbours. We can thus conclude that for *crowded* fields the use of small pixel scales down to 1.5 mas pix^{-1} is indeed important for keeping a high level of astrometric accuracy.

Combining all results for isolated and crowded sources, we can conclude the following for the design and the operation of MICADO.

(i) For sufficiently *isolated* target sources, pixel scales smaller than or equal 3 mas pix^{-1} are free of notable (≈1 μas) systematic uncertainties and suited for accurate astrometry. This scale is therefore going to be the standard pixel scale for MICADO.

(ii) For the special case of *crowded* sources, smaller pixel scales down to 1 mas pix^{-1} can substantially (factors ≈2) reduce the astrometric errors introduced by source overlap. We therefore implemented a 'small-scale mode' with a reduced pixel scale of 1.5 mas pix^{-1} into the MICADO design. This mode will be used to map very crowded regions.

4.2 Instrumental distortion

The geometric distortion of an optical system can seriously limit its astrometric accuracy. In the following, we discuss *non-linear* distortions. *Linear* terms like shifts, rotations, scalings, or shear, are absorbed by first (or higher) order coordinate transforms (see Section 3). In case of non-linear distortion, the effective pixel scale is a function of detector position (e.g. Greason et al. 1994, and references therein).

For MICADO, the amount of distortion to be expected (meaning the difference between imaged and theoretical image positions) is of the order of a few per cent. The largest numbers, about 5 per cent, we find for the case of an Offner design for the camera. Although other optical designs might have the potential to reduce the amount of distortion down to ≈0.3 per cent (Dierickx 2008), it cannot be neglected. Across a FOV of 1 arcmin, a distortion of 0.3 per cent corresponds to a misplacement of 0.18 arcsec. For comparison, an astrometric accuracy of ≈50 μas across the same FOV corresponds to a relative error of less than 10^{-6}. Such low uncertainties cannot be achieved by design. In order to reach the desired astrometric accuracies, the distortion must be compensated by dedicated calibration schemes – regardless of its amplitude.

Another effect to be considered is imperfect fabrication of the detectors. The Hawaii-4RG detectors to be used for MICADO are designed with pixels sizes of 15 μm. The position accuracy of these pixels in the detector grid is ≈10 nm; for a pixel scale of 3 mas pix^{-1}, this corresponds to an astrometric uncertainty of ≈2 μas (Richard

Blank[3], private communication), i.e. hardly notable. However, any distortion calibration scheme must provide the ability to catch potential inaccuracies of the detectors [see also Anderson 2002 for the case of *Hubble Space Telescope* (*HST*)/Wide Field Camera (WFC)].

Depending on the complexity of the distortion, two methods for its description are possible. *Analytic* descriptions make use of analytic parametrizations analogous to the coordinate transforms discussed in Section 3. Most commonly, two-dimensional polynomials up to about fifth order are used as distortion models (e.g. Greason et al. 1994, and references therein). This approach allows covering all effects up to a selected order without prior knowledge on the geometry of the problem. The disadvantage of this method is the large number of model parameters to be calculated. A recent example for this approach is the analysis of the nuclear star cluster of the Milky Way by Ghez et al. (2008) and Lu et al. (2009). They use a polynomial model to correct the geometric distortion of the Near-Infrared Camera (NIRC) and NIRC2 cameras at the W.M. Keck Observatory.

If a physical model for the distortion is at hand, a corresponding model can be substantially simpler. A recent example for this approach is the analysis of the nuclear star cluster of the Milky Way by Trippe et al. (2008) and Gillessen et al. (2009). They use the third-order model

$$\boldsymbol{r} = \boldsymbol{r}'(1 - \beta \boldsymbol{r}'^2) \tag{7}$$

with

$$\boldsymbol{r} = \boldsymbol{x} - \boldsymbol{x}_C \qquad \text{and} \qquad \boldsymbol{r}' = \boldsymbol{x}' - \boldsymbol{x}_C$$

(e.g. Jähne 2005)[4] in order to correct the distortion of the imager NAOS/CONICA at the VLT. Here, $\boldsymbol{x}$ and $\boldsymbol{x}'$ are the true and distorted image coordinates, respectively, β is a parameter describing the strength of the grid curvature and $\boldsymbol{x}_C \equiv (x_C, y_C)$ is the zero-point of the distortion on the detector. This approach has the obvious advantage that it requires only three parameters (β, x_C, y_C) for a third-order distortion model compared to 20 for the case of a full polynomial solution. The most important disadvantage is the need for accurate a priori knowledge of the distortion geometry.

In cases where analytic solutions are not feasible or not accurate enough, *empiric* descriptions might be used instead or in addition. This means that the information of interest is stored in lookup tables. Those tables usually have the dimensions of the detector(s) and give the amount of distortion (or correction) for each pixel (separately for x, y). This approach is necessary if a significant high-frequency distortion – meaning that the spatial scales of the signal are small compared to the detector size – is present. For the specific case of MICADO, the gaps between the detectors will introduce discontinuities into any astrometric solution. This effect could be caught by using lookup tables.

In a detailed analysis of the WFC instrument aboard the *HST*, Anderson (2002) uses a combined 'polynomial model plus lookup table' ansatz to model the distortion of the camera. He achieves residuals smaller than 0.01 pixels with this method. For the case of MICADO, this would mean residual errors below $\approx$30 μas which is an amount acceptable for our purpose.

There are several methods to extract the distortion parameters. *On-sky methods* make use of dedicated observations of astronomical targets; usually, star clusters are used (Anderson 2002). If the true (astrometric) coordinates of the sources in the target field are known, one can derive the distortion parameters by comparing true and observed (detector) positions. If the true source positions are not known, one can observe the target field many times with slightly different telescope pointings. In this case, one compares the pairwise distances of objects that are present in two or more images. Modulations in these distances as function of detector position are equivalent to (non-linear) distortion.

By construction, on-sky methods are sensitive to distortions introduced by the atmosphere. Given the high accuracies we seek, those methods are not practicable (at least stand-alone) for the case of MICADO but will be a secondary approach.

In-lab methods characterize the instrument with dedicated measurements in the laboratory or at the telescope. One example is the 'north–south test' used for the spectro-imager Spectrograph for Integral Field Observation in the Near-Infrared (SINFONI) at the VLT (e.g. Abuter et al. 2006). These methods use devices that illuminate the detectors with well-defined images or light patterns. Comparing the theoretical with the observed images allows for a description of the distortion.

Given that in our accuracy regime the atmosphere can severely limit the quality of on-sky calibration images (see Sections 4.4–4.8 for details), we assume that we need to implement an internal calibration device into MICADO. For this purpose, we examined the use of a calibration mask located in the focal plane of the imager. Such a mask could be a regular pattern of holes in an non-transparent material. However, the following calculation shows that this is actually challenging. With MICADO, we want to observe an FOV with extension $x = 1$ arcmin with an accuracy $\delta x = 10$ μas, meaning a relative accuracy of

$$\delta x/x \approx 1.7 \times 10^{-7}.$$

The width of MICADO's focal plane will be approximately $l = 0.25$ m. This scales to a positioning accuracy for any reference located in the focal plane of

$$\delta l = l \times \delta x/x \approx 4.2 \times 10^{-8}\text{m}.$$

As we see here, the positions of the holes in our calibration mask need be known with accuracies of about 40 nm (the hole diameters would be $\approx$30 μm corresponding to diffraction-limited point sources). This result does not mean that the fabrication process needs to be accurate at this level. Instead, it is sufficient to map the hole positions with accuracies of $\approx$40 nm after the making of the mask. State-of-the-art photolithographic techniques provide the required production and mapping accuracies at standard temperatures ($\approx$300 K). With this approach, the calibration mask would be a transparent quartz plate with a chrome cover into which the holes are etched. Although such a system is thermally very stable, the impact of possible non-linear thermal deformation needs to be investigated via dedicated laboratory experiments (B. Lorenz,[5] D. Rose[6], private communication). We consider the calibration mask approach to be the easiest one in terms of telescope and instrument design. We have not yet investigated in detail more 'exotic' ideas, e.g. illuminating the detectors with a well-defined diffraction pattern or spectrum.

As we see from the discussion in this section, it is crucial to gather the maximum amount of information on the instrumental distortion of MICADO. We therefore conclude that the following steps are necessary.

[3] Teledyne Imaging Sensors, Camarillo, USA.

[4] See also the electronic manual of the public Gemini North Galactic Center Demonstration Science Data Set for another application on Galactic Centre imaging data.

[5] Center for NanoSciences, Ludwig Maximilians University, Munich, Germany.

[6] Rose Fotomasken, Bergisch Gladbach, Germany.

(i) Estimating amount and geometrical structure of the distortion theoretically from the optics design.

(ii) Careful mapping of the camera in the lab and at the telescope. Implementation of an internal calibration device, e.g. a calibration mask.

(iii) Testing the system on-telescope for any evolution of the distortion. Evolution parameters can be time (aging effects), telescope orientation (gravitational flexure), etc.

(iv) Additional regular dedicated on-sky calibration observations of sufficient astronomical targets, e.g. star clusters, as secondary tests.

4.3 Telescope instabilities

Instabilities of the telescope system have the potential to affect astrometric experiments. For the present design of the E-ELT, one expects relative intranight plate scale variations of ≈0.1 per cent (Gonzalez 2008). Across an FOV of 1 arcmin, this corresponds to position variations of the order of 60 mas. Another effect are adapter–rotator instabilities that can introduce systematic frame-to-frame rotation. Those rotations introduce position misplacements of the same order of magnitude (see e.g. Trippe et al. 2008 for the case of VLT/NACO).

Fortunately, those effects – shifts, global scalings, rotations – are linear in geometry. Therefore, they can be controlled via coordinate transforms of first or higher order without additional calibration steps. This statement does not hold, however, for gravitational flexure effects that introduce a time-variable non-linear instrumental distortion. This phenomenon is covered by our discussion of instrumental distortion in the previous section.

4.4 Achromatic differential atmospheric refraction

Any ground-based position measurement is affected by atmospheric refraction. As we discuss relative position measurements of sources located in our FOV, we have to take into account any *relative* or *differential* atmospheric refraction. In this case, we have to discriminate achromatic and chromatic effects.

Achromatic differential refraction is caused by the slight difference in zenith angles ζ of two (or more) sources located within the same FOV. For each source, the atmospheric refraction leads to a deviation between physical and observed zenith angles. For two sources at slightly different zenith angles, those deviations will be different. Therefore, the observed distance between the two targets deviates from the physical one and needs to be corrected. The required correction Δx of the distance between two sources 0 and 1 is approximately given by the relation

$$\Delta x = \left(1 + \tan^2 \zeta_1\right) \left(A + 3B \tan^2 \zeta_1\right) \Delta\zeta. \quad (8)$$

Here, ζ_1 is the zenith angle of source 1, $\Delta\zeta$ is the *observed* zenith separation, A and B are constants. Detailed calculations (Gubler & Tytler 1998) show that the linear terms of this effect are of the order of several milliarcsec, whereas the quadratic terms are as small as ≈1 μas. For example, with $\zeta_1 = 45^\circ$ and $\Delta\zeta = 30$ arcsec, the correction amounts to ≈15 mas in the first-order terms and ≈2 μas in second order. Fortunately, these terms can be absorbed by quadratic coordinate transforms (see Section 3). From this, we conclude that we can neglect achromatic differential atmospheric refraction for the purpose of our analysis.

4.5 Chromatic differential atmospheric refraction

Chromatic differential refraction (CDR) or *atmospheric dispersion* is a more severe problem for accurate astrometry than the achromatic case. As the refractive index n of the atmosphere is a function of wavelength, the observed angular distance between two sources is a function of the (relative) source colours. For a given *true* zenith distance ζ_t, the deviation from the *apparent* zenith distance ζ_a (in radians) follows the approximative relation

$$\zeta_t - \zeta_a \simeq R \tan \zeta_t = \left(\frac{n^2 - 1}{2n}\right) \tan \zeta_t. \quad (9)$$

Here, R is the refraction constant. For standard conditions, the refractive index is given by

$$(n - 1) \times 10^6 = 64.328 + \frac{29\,498.1 \times 10^{-6}}{146 \times 10^{-6} - s^2} + \frac{255.4 \times 10^{-6}}{41 \times 10^{-6} - s^2} \quad (10)$$

with $s = \lambda^{-1}$, λ being the vacuum wavelength in nm (e.g. Cox 2000). Of course, this has an impact on relative astrometry only if the two sources have different colours. For observations of two stars with broad-band JHK filters, astrometric errors are of the order of 1 mas (within a wide range, depending on zenith angles, angular distances and source colours). We therefore need to correct the CDR in order to meet our desired accuracies.

In the following, we investigate the use of an atmospheric dispersion corrector (ADC) placed into the optical path. This ADC is a pair of ZnSe/ZnS biprisms which refracts – for a given zenith angle – the infalling radiation such that the CDR is compensated. In order to use this element for a range of zenith angles, the biprisms can be rotated around the optical axis relative to each other; this controls the strength of refraction. Such a system was built and operated successfully for the Sharp II+ NIR camera system (Eisenhauer 1998). The required optical components are available in the spatial dimensions needed for MICADO (S. Koebele private communication). In order to decide on the design strategy, we explored three options in detail:

(i) The use of one non-tuneable ADC optimized for simultaneous correction of the full wavelength band range *J, H*, K_s ($\lambda = 1.1, \ldots, 2.35$ μm).

(ii) One ADC covering the entire band range that can be tuned in wavelength to bands *J, H* and K_s, respectively.

(iii) Three ADCs, one for each of the three bands *J, H* and K_s.

For each option (1, 2, 3), we computed residual dispersions (dispersions left after correction) versus wavelength for each of the bands *J, H* and K_s. All calculations used zenith angles $\zeta = 45^\circ$. Our computations made use of numerical optimization routines implemented into the software package MATHEMATICA.[7] The results for *J* band are given in Fig. 4. Whereas option 1 results in a very asymmetric curve of correction, options 2 and 3 are very similar in shape and highly symmetric. As we see here, one can reduce the residuals by using an ADC specifically designed for the wavelength band analysed (option 3) by factors of about 10 compared to a tunable ADC (option 2). However, the impact on astrometry is actually given by the *relative* displacement of two sources with different colours. This means that the residual astrometric error is mainly controlled by the symmetry of the curves, not by their amplitudes or absolute levels.

[7] Wolfram Research, Inc., Champaign, IL, USA.

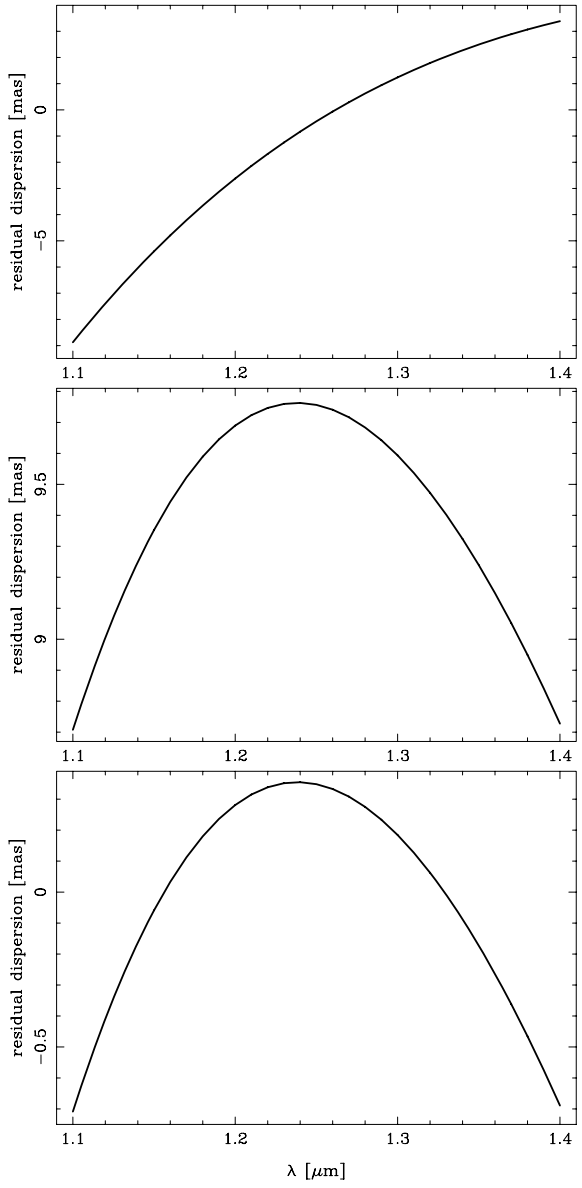

Figure 4. Residual dispersion vs. wavelength in *J* band after correction with an ADC assuming $\zeta = 45^\circ$. Top panel: using one non-tunable ADC for the entire *JHK* band range. Centre panel: using one tunable ADC for the entire JHK band range tuned to *J* band. Bottom panel: using an ADC specifically designed for optimum correction in *J* band. Please note the changes in scales. The non-tunable ADC results in a very asymmetric correction curve. The other two curves are offset by about 10 times their amplitudes from each other, but are very symmetric in their shapes.

We may therefore expect that options 2 and 3 result in very similar astrometric accuracies.

For a quantitative description of the residual astrometric errors, we analysed two hypothetical science cases. We examined

(i) an observation of two black bodies of very different temperatures ($T_1 = 3000$ K, $T_2 = 30\,000$ K), crudely corresponding to M5 and B0 main-sequence stars, respectively ('case A'),

(ii) the case of two black bodies at $T = 5800$ K (e.g. sun-like stars) affected by very different extinctions of $A_V = 25$ and 35, respectively ('case B'). For this case, we used the extinction law by Draine (1989) as taken from Lutz et al. (1996).

Table 2. Relative zenith angle shifts computed for the options, science cases, and filter bands discussed in the text. All numbers are in μas.

Band	*J*	*H*	K_s
Option 1			
Case A	730	73	196
Case B	642	112	250
Option 2			
Case A	9	9	6
Case B	35	23	21
Option 3			
Case A	9	9	2
Case B	35	22	11

For each option, science case, and filter band, we computed relative shifts in zenith angle between the sources 1 and 2 via

$$\Delta\zeta_{2-1} = \frac{\int \Delta\zeta(\lambda) S_\lambda \mathrm{d}\lambda}{\int S_\lambda \mathrm{d}\lambda}|_2 - \frac{\int \Delta\zeta(\lambda) S_\lambda \mathrm{d}\lambda}{\int S_\lambda \mathrm{d}\lambda}|_1. \quad (11)$$

We present the results of our analysis in Table 2. As we see here, using a non-tuneable ADC (option 1) for the entire *JHK* band range leaves us with errors of roughly ≈100 μas in *H* band which contains the centre of correction. When going to K_s and *J* bands, the residuals increase to ≈200 and 700 μas, respectively. All numbers exceed any acceptable value by factors of about 10 or more. This clearly rules out option 1.

Using a tuneable ADC (option 2) or three ADCs optimized for the three bands (option 3) reduces the residual zenith angle displacements to ≈10 μas. This result complies with our requirements and shows that our approach can indeed achieve the necessary accuracies for realistic science cases. As expected from equations (9) and (10), the errors increase with increasing frequency. Therefore, one should avoid observations at very short (shorter than *J*) wavelengths. Additionally, one should consider the use of narrow-band filters in case of (i) observations at short wavelengths or (ii) extreme relative source colours.

Another calibration step one should consider is an a posteriori correction. As we discuss above, the impact of CDR on astrometric solutions can be quantified analytically *if* the relative source colours are known. However, this requires careful monitoring of the atmosphere (see e.g. Helminiak 2009).

From our analysis of chromatic differential atmospheric refraction, we conclude the following.

(i) CDR distorts astrometric solutions by up to a few mas depending on source colours. We need to implement a dedicated correction.

(ii) Using a tuneable ZnS/ZnSe ADC reduces the astrometric signal caused by CDR to ≈10 μas in *JHK* bands assuming realistic science cases. We therefore highly recommend to implement such a device into MICADO.

(iii) In case of extreme relative source colours or observations at short (shorter than *J* band) wavelengths, one should consider the use of narrow-band filters additional to an ADC.

(iv) If the source colours and the atmospheric conditions (temperatures, pressures, humidities) are known with sufficient accuracies, one might additionally apply an analytic a posteriori correction of astrometric data.

4.6 Guide star measurement errors

MICADO's MCAO system is designed to make use of three natural guide stars that are located (at a priori arbitrary positions) in the FOV. Additionally, the use of six laser guide stars is foreseen. The stars are observed simultaneously as references for correcting the wavefront deformation imposed on astronomical signals by the atmosphere. The natural guide stars are used for correcting low-order effects, whereas the laser guide stars correct high-order distortions. The LGS high-order correction does not make use of the guide star positions.

This is different for the NGS low-order correction. This calibration step requires knowledge of the relative guide star positions. The guide star measurements will have finite errors due to atmospheric fluctuations that introduce a 'position wander'. Uncertainties in the measured guide star position will introduce time-variable distortion into the AO corrected FOV. For N stars, one may expect distortions up to order $N-1$, i.e. up to second order for the case of three natural guide stars. These distortions will differ from image to image. Therefore, it is necessary to combine images with full coordinate transform of minimum order two. If this is done, the effect will be compensated completely.

4.7 Differential tilt jitter

The light from a science target and the light from an adaptive optics system reference source travel through different columns of atmospheric turbulence. An AO system applies a tip-tilt correction to the signal received from the AO reference source. This correction is slightly different for other positions in the FOV. Therefore, any two objects in the observed field suffer from *differential tilt jitter*: a random, achromatic, anisotropic fluctuation of the observed angular distance of the two sources (e.g. Britton 2006; Cameron, Britton & Kulkarni 2009). In first order, the rms of this fluctuation follows the relation

$$\sigma_{TJ} \propto \theta \times D^{-7/6} \times \left(\frac{\tau}{t}\right)^{1/2}. \quad (12)$$

Here, θ is the angular distance between the sources, D is the telescope aperture, τ is the aperture wind crossing time (approximately: D divided by wind speed) and t is the integration time. Tilt jitter is an anisotropic effect with

$$\sigma_{\parallel} = \sqrt{3}\sigma_{\perp} \approx 1.732\sigma_{\perp}, \quad (13)$$

where $\sigma_{\parallel}, \sigma_{\perp}$ denote the tilt jitter rms parallel and perpendicular to the line connecting the two sources, respectively.

In Fig. 5, we give an example for a tilt jitter signal observed in images taken with an 8-m class telescope. This result is from the work by Fritz (2009) who analysed diffraction-limited VLT images of the nuclear cluster of the Milky Way. For pairs of stars, he computed the uncertainties of the measured distances parallel and perpendicular to the lines connecting the two stars. Fig. 5 shows the uncertainty as function of star angular distance. By means of linear fits, one finds a relation $\sigma_{\parallel}/\sigma_{\perp} = 1.91 \pm 0.22$, i.e. $\sqrt{3}$ within errors – as expected from equation (13). From the line slopes and the known integration times, one can estimate an aperture wind crossing time of $\tau \approx 0.6$ s. For details, refer to Fritz (2009) and Fritz et al. (2009).

The impact of this effect on astrometry can be substantial. To give a reference, based on observations with the Hale 200 inch telescope, Cameron et al. (2009) find astrometric uncertainties of $\approx$75 mas for $D = 5$ m, $\theta = 60$ arcsec and $t = \tau = 0.2$ s (i.e. $\tau/t = 1$). For a realistic intra-epoch E-ELT observation with $D = 42$ m and

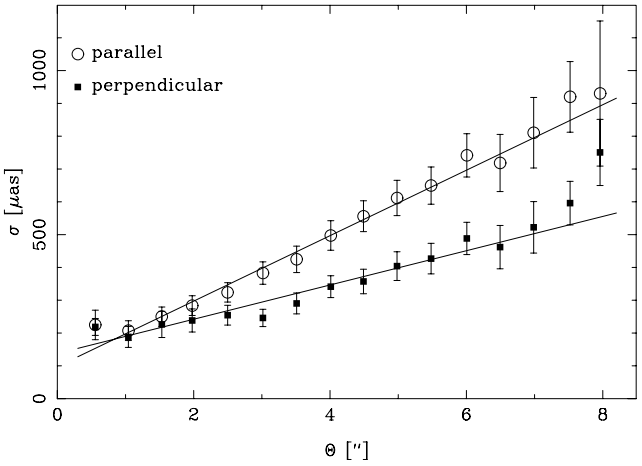

Figure 5. A differential tilt jitter signal as observed in VLT images. This diagram shows the error on the measured distance between two stars σ as a function of star angular distance θ. Errors are calculated parallel ($\parallel$) and perpendicular ($\perp$) to the line connecting the two stars on sky. Points with error bars are data, continuous lines indicate the best-fitting linear models. From the line slopes, one finds $\sigma_{\parallel}/\sigma_{\perp} = 1.91 \pm 0.22$, i.e. $\sqrt{3}$ within errors as expected from equation (13). This result is taken from Fritz (2009).

$t = 100\tau \approx 100$ s (i.e. $\tau/t = 0.01$), this scales to $\sigma_{TJ} \approx 600$ μas. Averaging out this error to reasonable scales (less than 50 μas) would take about 4 hours. This imposes severe constraints on any astrometric observation.

The calculation given above is strictly valid only for single-conjugate AO (SCAO) systems, i.e. AO systems using one reference source. However, MICADO is designed to use an MCAO system with three natural guide stars initially. The use of multiple guide star should reduce the tilt jitter error substantially. Ellerbroek (2007) finds that for a 30-m telescope and the case of three guide stars arranged in an equilateral triangle the error is reduced by a factor of $\approx$6 compared to the SCAO case. Scaling the results by Ellerbroek (2007) to the case of the E-ELT, one finds

$$\sigma_{TJ} \approx 430 \times t^{-1/2}\ \mu\text{as} \quad (14)$$

with t being the integration time in seconds and $\theta = 60$ arcsec. This means that accuracies of $\approx$10 μas can be achieved within integration times of about 30 min.

A helpful property of tilt jitter is the fact that it is random in time, but correlated in space. This is also reported by Fritz (2009) who finds that already using linear coordinate transforms between images reduces the error by a factor of $\approx$2. According to Cameron et al. (2009), the use of coordinate reference frames based on weighted pairwise distances between a target source and several reference sources is able to catch the tilt jitter error. This approach is similar to the concept of kriging (e.g. Clark & Harper 2000). It requires some tens of astrometric reference points in the FOV in order to obtain a sufficient number of pairwise baselines. Additionally, it requires any intra-epoch data set to consist of some tens of individual exposures instead of few long-term integrations. This is necessary in order to estimate the uncertainty (and thus the weight) of each pairwise source distance from its histogram. If this scheme is applied, the error can be reduced to $\approx$10 μas within few minutes of integration.

From our discussion on differential tilt jitter, we conclude for MICADO as follows.

(i) Differential tilt jitter can introduce errors of the order of $\approx$100 μas into typical E-ELT/MICADO observations. This effect

is not a challenge for the instrument design but for the planning of observations and data calibration.

(ii) The tilt jitter error integrates out with time as $\propto t^{-1/2}$. For the E-ELT, reducing the error to the order of $\approx$10 μas, integration times of at least $\approx$30 min per intra-epoch data set will be necessary.

(iii) The tilt jitter error can be calibrated out (down to $\approx$10 μas) by using dedicated astrometric reference frames and transforms. This requires (1) some tens of reference sources in the FOV and (2) some tens of individual exposures per intra-epoch data set.

4.8 Anisoplanatism

All existing AO systems suffer from *anisoplanatism*, meaning that the shape of a PSF is a function of its position in the FOV. Usually, this spatial variability is described by the relation

$$P(\theta) = P(0) * K(\theta) \tag{15}$$

(Fusco et al. 2000; Steinbring et al. 2002, 2005; Cresci et al. 2005). Here, θ is the angular distance from the centre of AO correction, $P(0)$ [$P(\theta)$] is the PSF at the centre of correction [at distance θ] and $K(\theta)$ is a kernel describing the PSF variation; $*$ denotes convolution.

If $K(\theta)$ were asymmetric then the centre of light of the PSF – and thus the detector position – would be a function of θ. This would introduce a systematic distortion of astrometric solutions that has to be calibrated out.

For existing SCAO systems, $K(\theta)$ is known to be symmetric. It can be approximated analytically as an elliptical Gaussian profile (e.g. Steinbring et al. 2005). In this case, the most important impact of anisoplanatism is a systematic degradation of the PSF's Strehl ratio S like

$$S(\theta) = S_0 \exp\left[-(\theta/\theta_N)^{5/3}\right] \tag{16}$$

assuming a perfect AO correction. Here, S_0 is the Strehl ratio at the centre of AO correction, the parameter θ_N is the anisopanatic angle. This effect reduces the SNR of a source and thus the statistical astrometric accuracy, but a priori does not introduce a systematic error.

For the case of MCAO systems with multiple centres of correction the problem is less well understood. In order to estimate the astrometric error introduced by anisoplanatism, we made use of preliminary simulations of multiguide-star Multi-Conjugate Adaptive Optics Relay (MAORY) PSFs in H and K bands[8]. The simulation data provide a grid of 217 PSFs located at distances between 0 and 80 arcsec from the centre of correction. The simulations assume a seeing of 0.6 arcsec. PSFs are sampled with pixel scales equal to $\lambda/2D$, corresponding to 4.05 and 5.30 mas pix^{-1} for H and K bands, respectively.

By construction, each PSF is centred accurately at the central pixel of a 512 × 512 pixel grid. As discussed above, we need to estimate the relative position error introduced by anisoplanatism. For this, we computed for each pair of PSFs a difference map by subtracting one PSF image from the other. In Fig. 6, we show the difference image for the case of two PSFs located 70 arcsec away from each other at positions (−60, 0) and (+10, 0) arcsec with the centre of AO correction located at (0, 0). Clearly, the map shows a complicated, highly symmetric light distribution. From the high degree of symmetry, one can already suspect qualitatively that the impact of MCAO anisoplanatism on the astrometry is small.

[8] Made available by the MAORY consortium at http://www.bo.astro.it/∼maory/Maory/

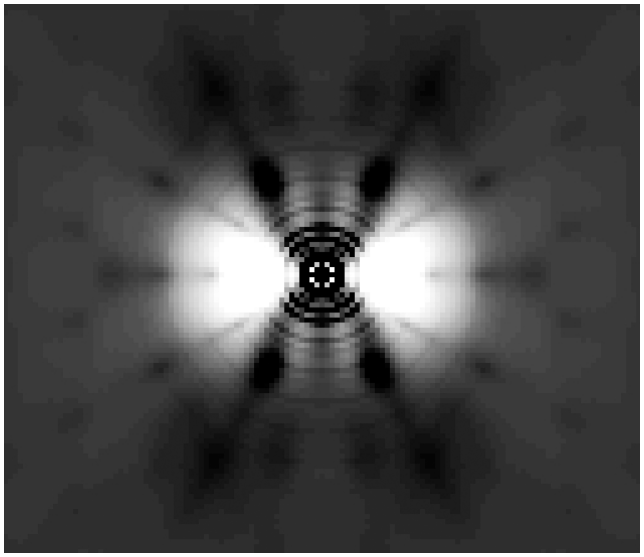

Figure 6. Difference image of two simulated MAORY K-band PSFs located 70 arcsec away from each other at opposite sides of the centre of AO correction. This image covers a field of $\approx$7.5 × 6 arcsec^2. The difference map shows a complicated, highly symmetric pattern.

In order to quantify this statement, we calculated for each difference map the centroid

$$x_{\rm centroid} = \frac{\sum_i x_i \cdot I_i}{\sum_i I_i} \tag{17}$$

of the light distribution. Here, x is an arbitrary coordinate, x_i and I_i are position and flux assigned to the ith pixel. The summation is performed over all map pixels (e.g. Berry & Burnell 2000). As we had 217 PSF images at hand, this procedure resulted in 23 436 measurements. Centroid positions different from the centre of the pixel grid correspond to position shifts of one PSF with respect to the other caused by asymmetries in the anisoplanatism kernel.

We summarize our results in Fig. 7. The histograms of the position shifts show quite sharp cut-offs at $\approx$7 μas in H band and at $\approx$8 μas in K band. We do not find a significant correlation of position errors with distance from the centre of correction or any other systematic relation.

We conclude that MCAO anisoplanatism probably introduces very small but notable uncertainties into astrometry. Depending on wavelength band, we find errors (upper ends of histograms) up to $\approx$8 μas. As the anisoplanatism effect is not (or very weakly) correlated with PSF positions in the FOV, it can probably not be caught by coordinate transforms or any other systematic correction but has to be included into the error budget.

4.9 High-z galaxies as reference sources

Throughout this article, we discuss *relative* astrometry, meaning measuring relative source positions. So far we implicitly assumed the reference sources to be point sources, especially stars. However, in some cases the use of reference points other than stars will be necessary.

(i) The number of stars located in the FOV can be too small. As discussed in Section 3, the number of reference sources is a function of the order of the coordinate transform used. For example, in case of a second-order transform, the minimum number is six. Using a larger number than the theoretical minimum is useful to average

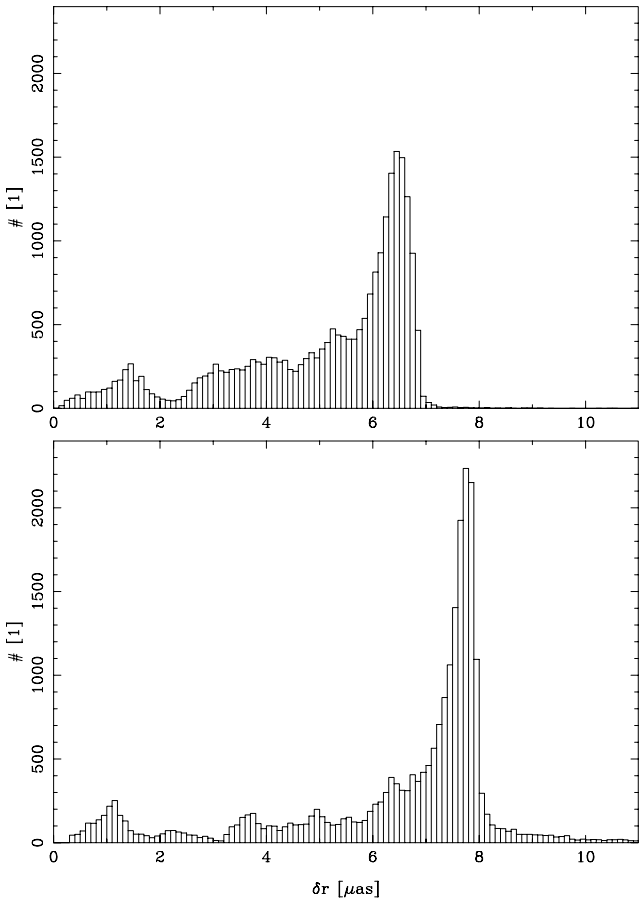

Figure 7. Astrometric errors introduced by MCAO anisoplanatism in *H* (top panel) and *K* (bottom panel) bands. Errors are centroid shifts (with respect to the case of perfectly symmetric light distributions) of the difference images between pairs of simulated PSFs located at different locations in the MAORY FOV. The histograms have cut-offs at ≈7 μas in *H* band and at ≈8 μas in *K* band.

out statistical position errors that could propagate into the transformation. Additionally, systematic effects like instrumental distortion (Section 4.2) and differential tilt jitter (Section 4.7) require large numbers of reference points for calibration purposes. Deep fields at moderate galactic latitudes ($|b| \approx 50^\circ$) include only a few to a few tens $K_{\rm AB} < 23$ stars arcmin^{-1} (see e.g. Förster Schreiber et al. 2006; Wuyts et al. 2008). This number is probably too small for astrometric MICADO observations.

(ii) The science case might require an extragalactic reference frame, thus excluding Galactic stars. For example, several groups (e.g. Bedin et al. 2003, 2006; Kalirai et al. 2004) use samples of background galaxies as reference in order to measure the absolute motion of globular clusters. Other science cases may need similar approaches (see Section 2).

In order to investigate the use of galaxies as references, we analysed two simulated MICADO deep field *K*-band images astrometrically. We simulated galaxies following realistic distributions of *K*-band magnitude as function of redshift *z* taken from the Chandra Deep Field South FIREWORKS ('field A'; Wuyts et al. 2008) and Faint Infrared Extragalactic Survey (FIRES) *Hubble Deep Field*-South ('field B'; Labbé et al. 2003) catalogues. All objects in the fields are built using four main ingredients.

(i) Smooth elliptical and disc galaxy light distributions with realistic surface number densities, sizes and $K - z$ distributions. The $K - z$ distributions were obtained by drawing at random galaxies from the two-source catalogues above, scaling the numbers by the ratio of the MICADO FOV and the respective survey areas. A fixed mix of ellipticals and discs was adopted (40/60 per cent), and effective radii were assigned at random so as to match approximately the size distributions of Franx et al. (2008). Uniform distributions are assumed for the axis ratios (with minimum of 0.3 for ellipticals and 0.1 for discs) and for the position angles.

(ii) Bulges (for disc galaxies) with de Vaucouleurs luminosity profiles adopted for simplicity. Bulge properties are poorly constrained at high redshift; our assumptions were guided by results from Elmegreen et al. (2009, and references therein; see also Genzel et al. 2008). We assumed uniform distribution of axis ratios between 0.7 and 1, position angles fixed at those of the host discs, effective radii inversely proportional to $1 + z$ such that $r_{\rm e} = 2$ kpc at $z = 0$ and a random distribution of bulge-to-total light ratios between 0 and 0.5.

(iii) Clumps (for disc galaxies) with realistic numbers per disc, typical light fractions, characteristic sizes and dependence on redshift, and radial distribution across the discs so as to roughly match observed properties at $z \approx 1$–2.5 (e.g. Genzel et al. 2008; Elmegreen et al. 2009 and references therein) and their lack at $z \approx 0$. Of the order of 1–10 clumps per disc were simulated, with Gaussian light profiles (again for simplicity), a narrow distribution of full width at half-maximum (FWHM) varying as $(1 + z)$ such that FWHM = 1 kpc at $z = 2.5$, light fractions of a few per cent typically, an exponential distribution of radial positions with scalelength five times that of the host disc, random position angles and axis ratios between 0.7 and 1.

(iv) Unresolved star clusters (for all galaxies). This is the ingredient which is least constrained at high redshift, as current instruments lack the resolution and point-source sensitivity to detect individual clusters if such exist at high *z*. To define their properties, we assumed superpositions of five different populations of point-like sources with a range of (Gaussian) magnitude and radial distributions. The brightest population contains the fewest clusters, with the most centrally concentrated distributions. The brightest cluster in each galaxy contributes 0.1 per cent of the total light. These assumptions roughly reproduce those of super star clusters and globular clusters in local galaxies, and unresolved sources in local analogues of $z \simeq 3$ Lyman-break galaxies (Overzier et al. 2008).

For each field image, we created three realizations corresponding to E-ELT/MICADO integration times of 1, 4 and 10 h, respectively, by adding Gaussian noise to the original map. As given by the input catalogues, field A has a point-source brightness limit of $K_{\rm AB} = 24.3$, field B of $K_{\rm AB} = 25.6$. These limits are 5σ depths for point sources in circular apertures of 2 arcsec diameter. In Fig. 8, we show four simulated galaxies from field B as examples.

The star clusters are especially interesting for astrometry. They provide an ensemble of several thousands of bright, point-like sources that can be analysed with standard tools developed for point-source astrometry. In each field, we selected all star clusters that were sufficiently isolated, meaning a distance of at least 30 mas (about three resolution elements) to the next source. In total, we used 1600 sources in field A and 2174 sources in field B. In each image, we fit the clusters with two-dimensional Gaussian brightness distributions in order to accurately (meaning few millipixels in the best cases) determine their positions. We then compared the results with the true source positions on the original noise-free maps. The

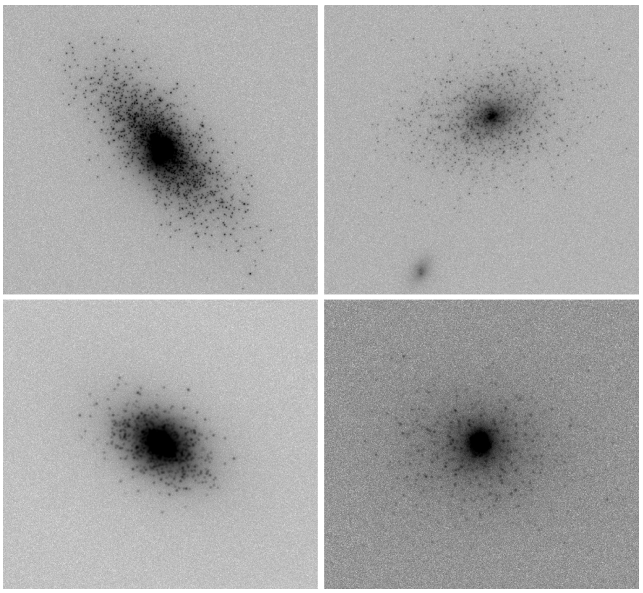

Figure 8. A few simulated galaxies from our artificial deep field B. Images in the top line cover ≈3.5 × 3.5 arcsec^2, images in the bottom line cover ≈1.8 × 1.8 arcsec^2.

distributions of the deviations between true and measured positions provide measures of astrometric accuracies.

We show the results for 10 h integration times in Fig. 9. For both the fields, we find distributions with 1σ widths of ≈920 μas (field A) and ≈650 μas (field B) per coordinate. These numbers correspond to the typical measurement accuracies for individual star clusters. The global astrometric accuracy is given by the standard error of the mean of the distribution, i.e. $\sigma/\sqrt{N}$ with N being the number of sources.

We summarize the astrometric accuracies found for all fields and integration times in Table 3. Not surprising, we find the highest accuracies of 23 and 14 μas (per coordinate) for fields A and B, respectively, for the largest integration time of 10 h. The errors increase to about 65 and 29 μas at integration times of 1 h. The systematic difference between fields A and B originates from their different depths: field B is based on a catalogue that has a ≈1.3 mag deeper brightness limit; it is therefore 'richer' of sufficiently bright targets. As MICADO will perform astrometric observations of sources $K_{AB} < 26$ (see also Section 1), the results found from field B are actually more realistic for describing the performance of MICADO. We can therefore conclude that total (i.e. the quadratic sum of the values for both coordinates) astrometric accuracies of ≈20 μas are realistic for integration times of order 10 h when using galactic star clusters as references.

So far, we have taken into account non-resolved (point-like) sources as references only. However, the global extended light distribution contains additional information. We therefore computed two-dimensional cross-correlations between different realizations of the same 'observations'. As reference, we used one 7000 × 7000 pixels (21 × 21 arcsec^2) subfield of field A containing seven galaxies. For each integration time (1, 4, 10 h), we computed three realizations of the random noise map added to the original light distribution. For all pairwise combinations, we computed the two-dimensional cross-correlations. We calculated their centres by means of two-dimensional Gaussian fits to the central parts of the cross-correlation maps. The uncertainty of the map centres provides a measure of astrometric accuracy. For all integration times we found very similar

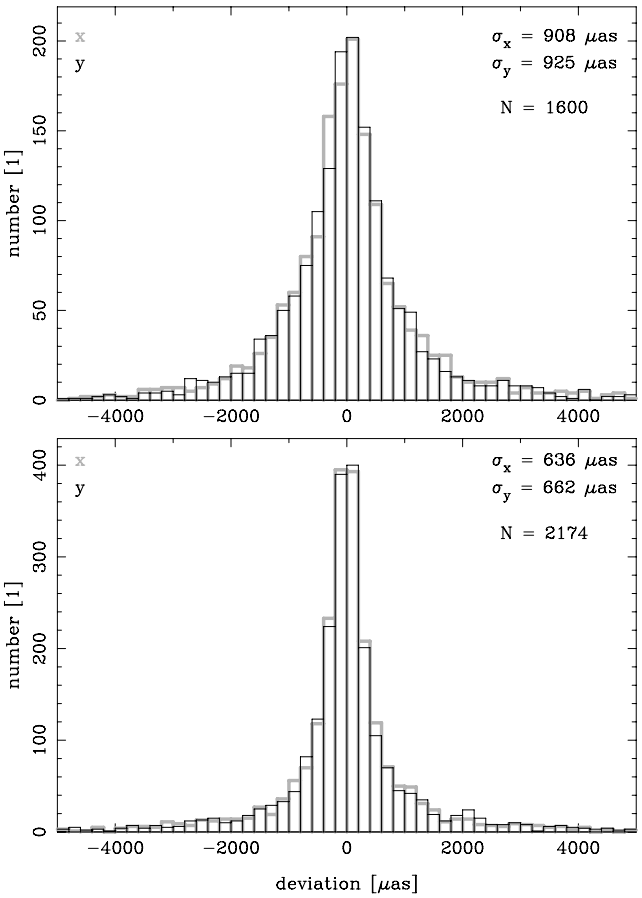

Figure 9. Histograms of position errors found from using several thousand point-like star clusters as references. These results are for fields A (top panel) and B (bottom panel) at 10 h integration time. Please note the different number axes scales.

Table 3. Astrometric accuracies found from using several thousand point-like star clusters as references. We give errors for the coordinates x and y as function of field and integration time.

	Field A		Field B	
t_{int} (h)	δx (μas)	δy (μas)	δx (μas)	δy (μas)
10	23	23	14	14
4	30	36	17	17
1	58	65	29	29

results: 4.5 μas at 1 h, 4.1 μas at 4 h, and 3.9 μas at 10 h. This indicates that at these level the accuracy is only weakly correlated with the SNR but dominated by systematic effects. In any case the impressive accuracies of ≈4 μas suggest that using two-dimensional cross-correlations of images can provide highly accurate astrometry.

However, two-dimensional cross-correlations cannot be used for relative astrometry in a straight forward manner. By construction, cross-correlations are only sensitive to shifts between images. They cannot describe transformations like scalings, rotations or higher order transforms as discussed in Section 3. Using them for astrometry therefore requires a more sophisticated approach than computing the cross-correlation between two (or more) images. One ansatz might be to calculate cross-correlations for a sufficient number (about ten

or more) of subfields of the target area. This would provide a set of relative position (changes). Feeding this data set into a proper model might result in a highly accurate coordinate transform.

From our analysis, we conclude that the use of high-z galaxies as astrometric calibrators is feasible at the level of $\approx$20 μas at integration times of about 10 h. This number assumes the use of several thousand point-like star clusters as reference sources (also assuming that such exist at intermediate-to-high redshift). Cross-correlation of images might provide even better accuracies, but would require a sophisticated computational scheme that can actually provide full coordinate transforms.

In some cases, one might consider separating the intra-epoch and the inter-epoch calibration steps. First, one can use a small number of stars (as discussed earlier, six may be sufficient) for *intra*-epoch (frame-to-frame) calibration. Proper adding of images allows building up SNR sufficient for detection of and position measurements on faint galaxies. Secondly, one can use these galaxies for *inter*-epoch calibration.

4.10 Calibration of the projected pixel scale

In Section 3, we have outlined the concepts of relative astrometry and coordinate transforms. These schemes make use of sets of reference positions $\{\boldsymbol{x}^n_{\rm ref}\}$ in order to compute transformation matrices for the nth data set. However, all transformation and calibration steps we have discussed up to now are executed in image space, i.e. in units of pixels. After removing non-linear distortions from the data, one needs to calibrate the pixel scale *as projected on sky* in order to accurately convert measured positions and motions into angular units. We note that the projected pixel scales for the two coordinates x, y may be different if the detector plane is tilted with respect to the focal plane.

Calculating the scaling factors requires astrometric reference points with known positions located in the target FOV. The number of reference sources should be at least three in order to allow for a full linear transformation. Fortunately, this calibration step needs to be executed only once for a selected "master' (or 'zero') image. All other images can be connected to the master image reference frame via coordinate transforms, including the proper scaling (e.g. Trippe et al. 2008). Errors on the reference positions propagate into the positions and motions calculated from the data. For the FOV of MICADO, reference position accuracies of order 1 mas translate into a *relative* scaling accuracy of

$$\delta x/x \approx 1\,{\rm mas}/53\,{\rm arcsec} \approx 2 \times 10^{-5}.$$

As discussed in Section 2, the science cases for E-ELT/MICADO demand accurate measurements of positions and proper motions over spatial scales from few ten μas (e.g. parallaxes of globular clusters; see Section 2.3) to few hundred mas (e.g. stellar orbits around Sgr A*; see Section 2.1). A relative pixel scale accuracy of 2×10^{-5} corresponds to an error of 10 μas over an angular distance of 500 mas. From this, we take the message that the accuracies of the reference positions should not exceed $\approx$1 mas substantially.

There are several possibilities for obtaining very accurate reference source positions. One of them is the use of sources located in the MICADO FOV and visible in both NIR and radio, e.g. QSOs or maser stars. If radio-interferometric positions (e.g. VLBI) – which are accurate on the sub-mas level – are at hand, the uncertainty on the pixel scale can be very low (see e.g. Reid et al. 2007 for the case of the Galactic Centre). Another option might be the use of stars from the *Hipparcos* catalogue (Perryman et al. 1997). However, the uncertainties in stellar proper motions, which are $\approx$0.8 mas yr^{-1}, will propagate into position uncertainties of $\approx$20 mas over a timeline of 25 years (given that the *Hipparcos* catalogue reference epoch is J1991.25; Perryman et al. 1997). This means that the astrometric uncertainties will exceed 10 μas if the spatial scale of the experiment is larger than $\approx$25 mas. A more promising approach is the use of data from the future *Gaia* astrometry space mission that will provide absolute astrometric accuracies well below 1 mas (Jordan 2008). The main advantage of the *Gaia* catalogue (its high accuracies aside) is the large number of stars included – $\approx 10^9$ – meaning that for any arbitrary field in the sky a sufficient number of reference points should be available.

We conclude from our discussion that for MICADO sufficient numbers of calibration sources with absolute position accuracies better than 1 mas will be available. We therefore expect that the calibration of the projected pixel scale introduces errors of $\approx$10 μas at most.

5 RESULTS AND ERROR BUDGET

We have identified and discussed 10 effects that might limit the expected astrometric accuracy of E-ELT/MICADO observations systematically. We have been able to quantify each of these sources of error. From this, we can calculate a prediction for the error budget of MICADO.

(i) For isolated point sources, *detector sampling/binning* does not introduce notable ($\approx$1 μas) errors as long as the pixel scale does not exceed 3 mas pix^{-1}. For sources affected by crowding, using a smaller scale of 1.5 mas pix^{-1} can improve the accuracy by factors of about 2 compared to the 3 mas pix^{-1} case. Therefore, MICADO will use a pixel scale of 3 mas pix^{-1} as standard and a reduced scale of 1.5 mas pix^{-1} for mapping crowded fields. For the error budget, we can thus assume a sampling error

$$\sigma_{\rm samp} = 1\,\mu{\rm as}.$$

(ii) Instrumental *geometric distortion* needs to be taken into account by dedicated calibration procedures. We propose to implement a calibration mask into MICADO that illuminates the detectors with a well-defined image. Such a mask would have to be mapped with accuracies of $\approx$40 nm. Based on our results in combination with published works using *HST* data, we estimate that distortion can be corrected down to levels of $\approx$10–30 μas. For the error budget, we therefore use

$$\sigma_{\rm dist} = 30\,\mu{\rm as}.$$

(iii) *Telescope instabilities*, notably plate scale instabilities and instrumental rotations, are linear effects that can be absorbed by coordinate transforms. Therefore, they do not contribute to the error budget.

(iv) Atmospheric *achromatic differential refraction* is important (order 10 mas) only in linear terms which can absorbed by coordinate transforms. Higher order contributions are of the order of 1 μas, meaning for the error budget

$$\sigma_{\rm ADR} = 1\,\mu{\rm as}.$$

(v) *Chromatic differential refraction* introduces position errors of the order of $\approx$1 mas in NIR observations depending on relative source colours. A tuneable ZnS/ZnSe ADC can reduce this effect to $\approx$10–20 μas for 'typical' science cases. Extreme relative source colours might require the additional use of narrow-band filters and/or analytic a posteriori correction schemes. For the error budget, we thus set

$$\sigma_{\rm CDR} = 20\,\mu{\rm as}.$$

(vi) AO *guide star measurement errors* for N natural guide stars can introduce distortions up to order $N - 1$ into images, meaning second-order distortions for the three NGS of MICADO. This effect can be absorbed by coordinate transforms (of order $N - 1$). It therefore does not contribute to the error budget.

(vii) Atmospheric *differential tilt jitter* can introduce errors of $\approx$100 μas into diffraction-limited E-ELT observations. It integrates out with $t^{-1/2}$. For MICADO which uses an MCAO system, the tilt jitter error can be integrated down to $\approx$10 μas within about 30 min of observation. Using dedicated coordinate transform allows reaching this accuracy in shorter times. For the error budget, we thus set

$$\sigma_{\rm TJ} = 10\,\mu{\rm as}.$$

(viii) The *anisoplanatism* of the MAORY AO system introduces uncertainties of up to $\approx$8 μas. There appears to be no correlation of this error with the position of a PSF in the FOV; it therefore cannot be calibrated out in a straightforward manner. Therefore, we add it to the error budget:

$$\sigma_{\rm aniso} = 8\,\mu{\rm as}.$$

(ix) Depending on target field and science case, the use of *galaxies as astrometric calibrators* may be necessary. From a simulated MICADO deep field, we find that we can use several thousand non-resolved galactic star clusters as point-like reference sources. However, good accuracies of $\approx$20 μas require long intra-epoch integration times of about 10 h; we consider this to be a somewhat large but realistic time-scale. We therefore use for the error budget:

$$\sigma_{\rm galaxies} = 20\,\mu{\rm as}.$$

(x) The accuracy of the *sky-projected pixel scale* is limited by the accuracy of astrometric positions of reference sources in the FOV. Given the typical accuracies of present-day radio-interferometric data and the future *Gaia* catalogue, which are better than $\approx$1 mas, we add to the error budget

$$\sigma_{\rm scale} = 10\,\mu{\rm as}.$$

From the individual uncertainties listed above, we can calculate a total intrinsic astrometric accuracy for MICADO as

$$\sigma_{\rm sys} = \sqrt{\sum_i \sigma_i^2} = 44\,\mu{\rm as}. \quad (18)$$

This number provides a systematic limit for astrometric accuracies to be expected from MICADO data. Of course, this result corresponds to a somewhat arbitrary 'typical' case. As many parameters like integration times, source colours, numbers and types of reference sources, etc. can vary over wide ranges, the actual $\sigma_{\rm sys}$ for a specific observation can be quite different – in both the directions – from the one we quote here. Nevertheless, we conclude that we are able to quantify the mean systematic astrometric accuracy achievable with MICADO which is $\approx$40 μas.

When discussing the accuracy of the measurement for a given target, one of course needs to add the statistical measurement error $\sigma_{\rm L}$ (equation 5) which scales with the SNR. For SNR = 100, $\sigma_{\rm L} =$ 34 μas, and thus the combined error is $\sqrt{\sigma_{\rm sys}^2 + \sigma_{\rm L}^2} = 56\,\mu{\rm as}$. SNR different from 100 modify this number accordingly.

6 CONCLUSIONS

In this article, we have studied the capabilities expected for the NIR imager MICADO for the future 42-m E-ELT with respect to accurate astrometry. A variety of science cases requires long-term astrometric accuracies of $\approx$50 μas. We discuss and quantify 10 effects that potentially limit the astrometric accuracy of MICADO. We conclude that the systematic accuracy limit for astrometric observations with MICADO is $\sigma_{\rm sys} \approx 40$ μas. We find that astrometry at this accuracy level with MICADO requires the fulfillment of several conditions.

(i) All images, regardless of their distance in time, need to be combined via full coordinate transforms of second order or higher.

(ii) MICADO needs to be equipped with an astrometric calibration mask for monitoring the instrumental distortion. The pixel scale of the camera should not exceed the 3 mas pix^{-1} used in the current design.

(iii) Astrometric observations require decent integration times of at least 30 min per epoch. This is unavoidable in order to average out atmospheric tilt jitter. When using high-z galaxies as astrometric reference points, integration times up to about 10 h can be necessary.

It is noteworthy that the effects discussed in this article already affect observations collected with present 8-m class telescopes. In his exhaustive analysis of NIR images obtained with VLT/NACO, Fritz (2009) has been able to detect signatures of CDR and differential tilt jitter in his astrometric data set. He concludes that taking into account these effects can improve the accuracies down to few hundred μas. This agrees with the findings of Lazorenko (2006) and Lazorenko et al. (2007) who analyse seeing-limited optical R-band ($\lambda_{\rm centre} = 655$ nm) images taken with VLT/FORS1+2. They conclude that they are able to achieve astrometric precisions (but not accuracies) of $\approx$100 μas by using a special scheme for scheduling observations and dedicated coordinate transforms (although they neglect instrumental geometric distortion).

The analysis we provide here is set up for the specific case of E-ELT/MICADO, but parts of our results are valid in general. This study should thus contain valuable information for other future 30–40-m telescopes. As some of the effects we discuss are actually observed in present-day 8-m class telescope data, our analysis might also be helpful for the calibration of data already taken. We therefore expect that our work is of interest well beyond the E-ELT community.

ACKNOWLEDGMENTS

We are grateful to the members of the MAORY consortium for providing us with simulated MCAO PSFs. NMFS gratefully acknowledges support from the Minerva Program of the Max-Planck-Gesellschaft. Last but not the least, we thank the anonymous reviewer whose comments were helpful to improve the quality of this article.

REFERENCES

Abuter R., Schreiber J., Eisenhauer F., Ott T., Horrobin M., Gillesen S., 2006, New Astron. Rev., 50, 398

Anderson J., 2002, in Arribas S., Koekemoer A., Whitmore B., eds, Proceedings of the 2002 HST Calibration Workshop. Space Telesc. Sci. Inst., Baltimore, p. 13

Anderson J., King I. R., 2000, PASP, 112, 1360

Anderson J., van der Marel R. P., 2009, ApJ, submitted

Anderson J., Bedin L. R., Piotto G., Yadav R. S., Bellini A., 2006, A&A, 454, 1029

Bedin L. R., Piotto G., King I. R., Anderson J., 2003, AJ, 126, 247

Bedin L. R., Piotto G., Carraro G., King I. R., Anderson J., 2006, A&A, 460, L27

Bender R. et al., 2005, ApJ, 631, 280

Berry R., Burnell J., 2000, Handbook of Astronomical Image Processing. Willman-Bell, Richmond, VA
Britton M. C., 2006, PASP, 118, 885
Cameron P. B., Britton M. C., Kulkarni S. R., 2009, AJ, 137, 83
Clark I., Harper W., 2000, Practical Geostatistics, pub. Geostokos
Cox A. N. (ed.) 2000, Allen's Astrophysical Quantities, 4th edn. Springer, New York
Cresci G., Davies R. I., Baker A. J., Lehnert M. D., 2005, A&A, 438, 757
Dierickx P., 2008, EELT Optical Design Report, ESO document E-TRE-ESO-227-138 (issue 3)
Diolaiti E., Bendinelli O., Bonaccini D., Close L., Currie D., Parmeggiani G., 2000, A&AS, 147, 335
Diolaiti E. et al., 2008, Proc. SPIE, 7015, 70150U
Draine B. T., 1989, in Kaldeich B. H., ed., Proc. 22nd ESLAB Symp. on IR Spectroscopy in Astronomy, ESA SP-290. ESA, Noordwijk, p. 93
Edberg S. J., Traub W. A., Unwin S. C., Marr J. C., IV, 2007, Acta Astronautica, 61, 52
Eisenhauer F., 1998, PhD thesis, Ludwig-Maximilians-University Munich
Ellerbroek B. L., 2007, TMT document TMT.AOS.TEC.07.038.REL01
Elmegreen B. G., Elmegreen D. M., Fernandez M. X., Lemonias J. J., 2009, ApJ, 692, 12
Förster Schreiber N. M. et al., 2006, AJ, 131, 1891
Franx M., van Dokkum P. G., Schreiber N. M. F., Wuyts S., Labbé I., Toft S., 2008, ApJ, 688, 770
Fritz T. K., 2009, MSc thesis, Ludwig-Maximilians-University Munich
Fritz T. K. et al., 2009, MNRAS, in press
Fusco T., Conan J.-M., Mugnier L. M., Michau V., Rousset G., 2000, A&AS, 142, 149
Genzel R. et al., 2003, ApJ, 594, 812
Genzel R. et al., 2008, ApJ, 687, 59
Ghez A. M. et al., 2005, ApJ, 635, 1087
Ghez A. M. et al., 2008, ApJ, 689, 1044
Gillessen S., Eisenhauer F., Trippe S., Alexander T., Genzel R., Martins F., Ott T., 2009, ApJ, 692, 1075
Gilmozzi R., Spyromilio J., 2008, in Stepp L. M., Gilmozzi R., eds, Proc. SPIE Vol. 7012, Ground-based and Airborne Telescopes II. SPIE, Bellingham, p. 701219
Gonzalez J. C., 2008, ESO document E-ICD-ESO-284/586-NNNN issue 1D.3
Greason M. R., Offenberg J. D., Cornett R. H., Hill R. S., Stecher T. P., 1994, PASP, 106, 1151
Gubler J., Tytler D., 1998, PASP, 110, 738
Helminiak K. G., 2009, New Astron., 14, 52
Jähne B., 2005, Digital Image Processing, Springer-Verlag, Heidelberg
Jordan S., 2008, Astron. Nachrichten, 329, 875
Kalirai J. S. et al., 2004, ApJ, 601, 277
Labbé I. et al., 2003, AJ, 125, 1107
Lazorenko P. F., 2006, A&A, 449, 1271
Lazorenko P. F., Mayor M., Dominik M., Pepe F., Segransan D., Udry S., 2007, A&A, 471, 1057
Lindegren L., 1978, in Prochazka F. V., Tucker R. H., eds, Proc. IAU Colloq. Modern Astrometry. Institut fuer Astronomie, Vienna, p. 197
Liske J., 2008, E-ELT Imaging ETC: Detailed Description
Lu J. R., Ghez A. M., Hornstein S. D., Morris M. R., Becklin E. E., Matthews K., 2009, ApJ, 690, 1463
Lutz D. et al., 1996, A&A, 315, L269
Maillard J. P., Paumard T., Stolovy S. R., Rigaut F., 2004, A&A, 423, 155
Minowa Y. et al., 2005, ApJ, 629, 29
Montenbruck O., Pfleger T., 1989, Astronomie mit dem Personal Computer. Springer-Verlag, Heidelberg
Neumayer N., Cappellari M., Reunanen J., Rix H. W., van der Werf P. P., de Zeeuw P. T., Davies R. I., 2007, ApJ, 671, 1329
Noyola E., Gebhard K., Bergmann M., 2008, ApJ, 676, 1008
Overzier R. et al., 2008, ApJ, 677, 370
Perryman M. A. C. et al., 1997, A&A, 323, L49
Portegies Zwart S. F., Baumgardt H., McMillan S. L. W., Makino J., Hut P., Ebisuzaki T., 2006, ApJ, 641, 319
Reid M. J., Menten K. M., Trippe S., Ott T., Genzel R., 2007, ApJ, 659, 378
Renzini A., 2008, MICADO Phase A Scientific Analysis Report, ESO document E-TRE-MIC-561-0007
Steinbring E. et al., 2002, PASP, 114, 1267
Steinbring E., Faber S. M., Macintosh B. A., Gavel D., Gates E. L., 2005, PASP, 117, 847
Strigari L. E., Bullock J. S., Kaplinghat M., 2007, ApJ, 657, L1
Trippe S., 2008, PhD thesis, Ludwig-Maximilians-University Munich
Trippe S. et al., 2008, A&A, 492, 419
Valentijn E. A. et al., 2007, in Shaw R. A., Hill F., Bell D. J., eds, ASP Conf. Ser. Vol. 376, Astronomical Data Analysis Software and Systems XVI. Astron. Soc. Pac., San Francisco, p. 491
Wuyts S., Labbé I., Schreiber N. M. F., Franx M., Rudnick G., Brammer G. B., van Dokkum P. G., 2008, ApJ, 682, 985
Yano T., Gouda N., Kobayashi Y., Yamada Y., 2007, Advances Space Res., 40, 664
Zoccali M. et al., 2003, A&A, 399, 931

This paper has been typeset from a TEX/LATEX file prepared by the author.